Interferometric methods for radiometric temperature sensing

J. Howard
Plasma Research Laboratory,
Australian National University. Canberra ACT 0200

Abstract

We describe a wide field-of-view large aperture electro-optically modulated infrared filter spectrometer (MIRF) for estimation of absolute blackbody temperatures. Based on electro-optic lithium niobate crystals, and thermally compensated wave-plates, the phase of interference fringes generated by the electro-optic modulation can be related directly to the blackbody radiation temperature, without regard to the spatial variation of the surface emissivity or need for absolute sensitivity calibration. When combined with a mid-IR imaging camera and appropriate software, the system can, in principle, deliver time resolved temperature contours of the radiating body. As with other techniques that rely on spectral shape estimation of the temperature, the MIRF spectrometer is not as sensitive to temperature changes as a brightness radiometer. However, for high resolution applications, the filter can be used for in-line routine absolute calibration of sensitive IR cameras that sense only "brightness temperature" variations. We describe single channel and imaging instruments that can be configured for estimating blackbody temperatures from emission peaking in the infrared through to visible.

1 Introduction

Non-contact optical thermometry is a rapidly growing field with applications in remote-sensing of hostile or corrosive environments, medical imaging, environmental studies and industrial process monitoring. Although the current state-of-the-art relies on cryogenic radiometers, uncertainties related to details of surface emissivity pose a problem for accurate absolute temperature estimation in many applications.

The blackbody spectral radiance is a universal single parameter distribution governed by the temperature T of the radiating source (see Fig. 1):

$$H_\nu(\nu;T) = \frac{2h\nu^3}{c^2}\frac{1}{\exp\left(h\nu/kT\right)-1}. \tag{1}$$

Integrated over wavelength, the total power radiated by a surface of area A and emissivitiy ϵ at temperature T is given by

$$P = \epsilon A\sigma T^4 \tag{2}$$

where σ is the Stefan-Boltzmann constant. In general, the emissivity $\epsilon(\nu, T)$ can be dependent on both wavelength and temperature. Within a narrow fixed wavelength band, the emission intensity is a strong function of temperature. Based on this fact, narrowband radiometric methods for temperature estimation require knowledge of the absolute sensitivity of the detection system as well as an estimate of the surface emissivity. Absolute infrared radiometers thus measure the"brightness temperature" of a radiating body. This is equal to the physical temperature for a perfect blackbody (an object with 100% emissivity), but is less than the physical temperature for an object with lower emissivitiy.

An alternative method to estimate temperature absolutely is to fit the spectral shape of the blackbody curve, or to accurately estimate the wavelength of peak emission λ_M given by Wein's displacement law

$$\lambda_M T = 2.898 \times 10^{-3}\ \mathrm{m\,K}. \tag{3}$$

This approach relies on being able to treat the radiation source as a greybody in the sense that the spectral variation of the emissivity is unimportant in the region of interest. Standard spectral techniques for estimation of source temperatures include Fourier-transform infrared (FTIR) spectroscopy, optical pyrometry and two-color radiometry. Though not as sensitive to small temperature changes as radiometers, spectral techniques are now achieving sub-degree temperature resolution [1].

In this work we consider the utility of electro-optic polarization interferometers for relatively low resolution spectral applications such as the measurement of broadband infrared blackbody radiation. The modulated infrared filter spectrometer (MIRF spectrometer) is based on electro-optically modulatable lithium niobate crystals and fixed delay waveplates set between polarizing plates. It monitors the low order spectral moments of the emission spectrum within a given passband. These moments are sensitive to the radiating source temperature. MIRF is an extension of the high resolution MOSS spectrometer [2] to broadband applications. The so-called MOSS (modulated optical solid-state) spectrometer monitors the complex coherence (fringe visibility and phase) of an isolated spectral line at one or more optical delays and has been used recently for visible light Doppler imaging of high temperature plasmas in the H-1 heliac [3].

Since it is a spectrally discriminating device, MIRF does not require absolute intensity calibration as is the case for radiometric based instruments such as IR cameras. On the other hand it is much simpler and more compact than Fourier transform infrared (FTIR) spectrometers to which it is related. It is easily adapted for the absolute calibration of imaging infrared cameras and is less susceptible to the drifts, ambient noise and or long-term stability problems associated with Michelson FTIR interferometers. The MIRF Spectrometer is a relatively inexpensive, compact, robust and portable instrument for spectral determination of absolute temperature images for condition monitoring of furnaces

and kilns as well as remote inspection, for example, of plasma facing components and antenna systems in fusion devices.

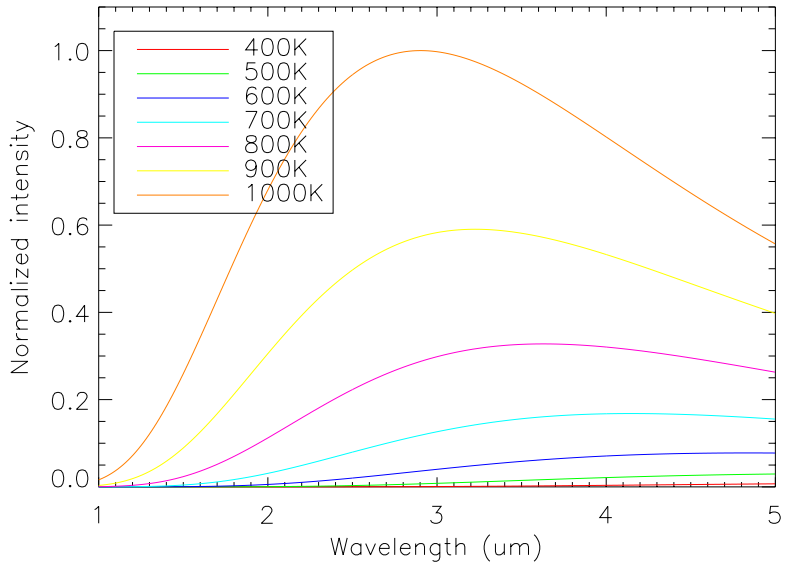

(a)

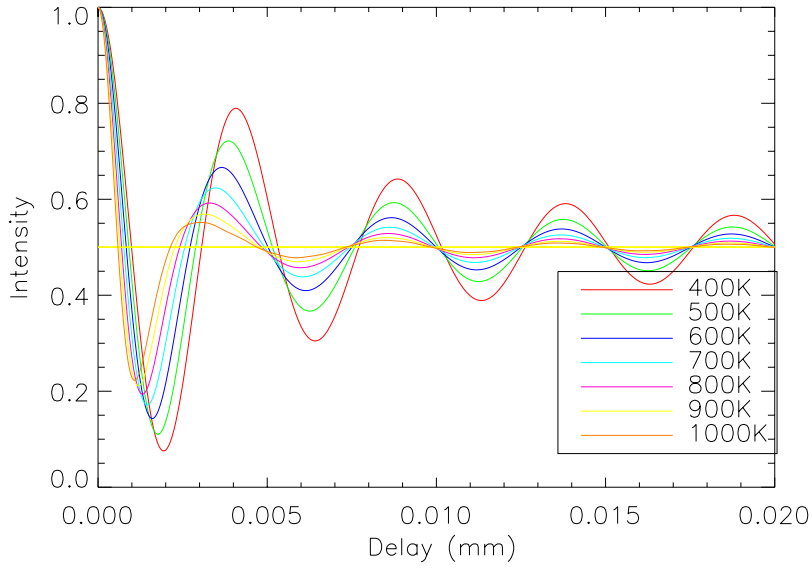

(b)

Figure 1: (a) Blackbody emission spectrum in the 1-5 μm band for temperatures spanning the range 400-1000K (b) Fourier transform of the emission spectra in (a). A top-hat bandpass filter spanning the range 1-5 μm has been applied. The delay coordinate is expressed in terms of an equivalent free-space interferometer mirror separation

2 Absolute radiometry

Introducing the dimensionless parameter $x = h\nu/kT = hc/\lambda kT$, the blackbody spectrum can be expressed as

$$H_\nu(\nu;T) = aT^3 H(x) \tag{4}$$

where a is a constant and the universal spectral dependence is captured by the function

$$H(x) = \frac{x^3}{\exp x - 1}. \tag{5}$$

This distribution is shown in Fig. 2(a). If the source temperature increases incrementally by ΔT, the radiant intensity also increases such that

$$\frac{\Delta H_\nu}{H_\nu} = \rho(x)\,\frac{\Delta T}{T} \tag{6}$$

where

$$\begin{aligned} \rho(x) &\equiv \frac{T}{H_\nu}\frac{\partial H_\nu}{\partial T} \\ &= \frac{x \exp x}{\exp x - 1} \end{aligned} \tag{7}$$

is the normalized differential radiometric temperature sensitivity. Note from Fig. 2(b) that $\rho(x) \approx x$ is an excellent approximation over much of the spectrum.

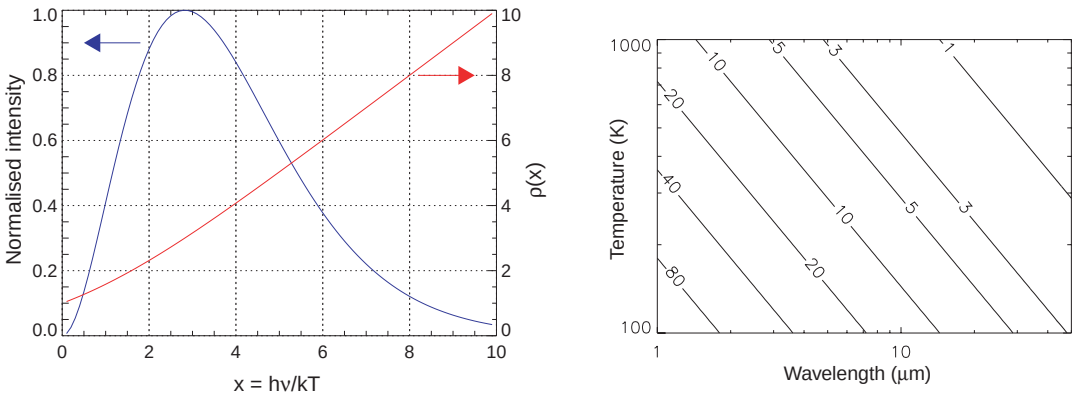

(a) (b)

Figure 2: (a) Variation of universal blackbody spectrum and the radiometric temperature sensitivity factor $\rho(x)$ as a function of dimensionless parameter $x = h\nu/kT$. (b) Contours of the parameter x versus radiation wavelength and source temperature.

If the emissivity factor is included, the dependence of the temperature uncertainty ΔT_R on errors in the estimated emissivity is given by

$$\frac{\Delta\epsilon}{\epsilon} = \rho(x)\,\frac{\Delta T_R}{T}. \tag{8}$$

This shows that the sensitivity to emissivity variations is weaker for blue side measurements (x large). However, moving further into the blue reduces the radiant power and increases the influence of noise sources. With $\gamma_R = \Delta T_R/T$ as a measure of the radiometer sensitivity, and taking the minimum measureable intensity variation $\Delta I = \Delta H_\nu \Delta\nu$ to be set by the rms noise level ε in the band $\Delta\nu$, the maximum sensitivity is obtained when $\partial\gamma_R/\partial x = 0$ and occurs for $\rho \approx x = 4$. Under optimum conditions, Eq. (8) shows that a 10% inaccuracy in the estimate of emissivity can give rise to not insubstantial errors of order a few percent in the inferred temperature.

To overcome these problems as well as issues relating to absolute calibration, it is possible to infer temperature by measuring the ratio of the radiation intensity at two independent wavelengths and using Planck's radiation law [Eq. (1)]. This approach obviates the need for knowledge of the emissivity or its temperature variation, but requires either for the body to be grey $\epsilon(\nu) = \epsilon$ or for the spectral dependence of ϵ (the slope) to be known. As well as reduced sensitivity to emissivity, ratio thermometers are largely insensitive to obscuration of the field-of-view due, for example, to dust, smoke, obstruction or lens contamination.

3 Spectral methods

Because of the slowly varying nature of the blackbody spectrum, accurate estimation of λ_M requires measurements over a significant spectral region. On the other hand, by the complementarity of time and frequency domain systems, shifts in λ_M are manifest over a small range of optical delay that can be probed interferometrically. Since the spectral bandwidth required to characterise the blackbody temperature is wide ($\Delta\nu/\nu \gtrsim 0.1$), the temporal coherence is small and most of the spectral information resides in the interferogram close to zero delay.

Fourier transform infrared spectrometers (FTIR), usually configured as Michelson interferometers, are often employed for the estimation of blackbody temperatures [4]. The ideal FTIR signal intensity (interferogram) can be expressed as

$$S_\pm(\tau) = \frac{I_0}{2}\Big[1 \pm \Re[\gamma(\tau)]\Big] \tag{9}$$

where I_0 is the spectrally integrated emission intensity, τ is the optical path time delay between interfering wavefronts and $\gamma(\tau)$ is the optical coherence, related to the light spectral radiance $H_\nu(\nu)$ through the Weiner-Khinchine theorem

$$\gamma(\tau) = \frac{1}{I_0}\int_{-\infty}^{\infty} H_\nu(\nu)\exp(\mathrm{i}2\pi\nu\tau)\,\mathrm{d}\nu. \tag{10}$$

In practice, the maximum fringe visibility (at $\tau = 0$) is reduced by the instrument spectral repsonse to less than unity. This is accounted by multiplying the complex coherence γ by the instrument coherence $\gamma_I = \zeta_I \exp(\mathrm{i}\phi_I)$ where $\zeta_I < 1$ is the

instrument contrast and ϕ_I the instrument phase. Unless otherwise indicated, we hereafter take $\zeta_I = 1$.

Figure 1(b) shows the computed Fourier transform of the blackbody spectra of Fig. 1(a) after windowing by a top-hat filter of spectral passband 1-5 μm. As expected, the first zero of the interferogram around 1 μm pathlength delay, shifts to smaller delays as temperature increases (λ_M decreases). Also note that the fringe visibility decreases at higher temperatures (more of the passband is filled). For small interferometer delays, the blackbody interferogram exhibits a smooth and regular variation with temperature. Thus, the first spectral moment of the radiation received in a given spectral passband (related to λ_M), is conveyed by a single measure of the interferogram, namely its slope at the first zero crossing. The effective spectral width of the received radiation is carried by the curvature (second derivative) of the interferogram fringe envelope n Figure 1(b) shows the computed Fourier transform of the blackbody spectra of Fig. 1(a) after windowing by a top-hat filter of spectral passband 1-5 μm. As expected, the first zero of the interferogram around 1 μm pathlength delay, shifts to smaller delays as temperature increases (λ_M decreases). Also note that the fringe visibility decreases at higher temperatures (more of the passband is filled). For small interferometer delays, the blackbody interferogram exhibits a smooth and regular variation with temperature. Thus, the first spectral moment of the radiation received in a given spectral passband (related to λ_M), is conveyed by a single measure of the interferogram, namely its slope at the first zero crossing. The effective spectral width of the received radiation is carried by the curvature (second derivative) of the interferogram fringe envelope near zero delay. Both of these quantities vary with temperature. ear zero delay. Both of these quantities vary with temperature.

We show below that the interferogram phase is a sensitive measure of the source temperature. The temperature-dependent shift in the interferogram zero-crossing phase can be monitored by modulating the interferometer path difference about an appropriate offset and measuring the ratio of modulation depth (fundamental amplitude) to average light intensity (dc). Alternatively, by sinusoidally modulating about a turning point, small changes in temperature are revealed as a change in the signal harmonic content. In this latter case, the temperature information is encoded at fundamental and second harmonic frequencies, away from low-frequency "$1/f$" flicker noise. Perhaps more importantly, taking the ratio of harmonic terms eliminates the need for knowledge of the instrument function ζ_I. Finally, as an interferometric version of a two-colour ratio thermometer, we also explore "interferometric ratio" methods involving the superposition and beating of interferograms in different wavelength bands.

superposition and beating of interferograms in different wavelength bands. onents so that a well-defined portion of the incident radiation

4 MIRF construction

For optimum performance, Michelson interferometers must be carefully aligned. They can also be bulky and sensitive to external noise, and require a computer for inversion/display of the interferogram. FTIRs usually require path length monitoring using a suitable fixed wavelength source such as a laser, while time resolution is limited by the duration of the mirror scan.

In order to overcome problems relating to mechanical and thermal stability as well as vibrations and acoustic noise in obtaining an estimate of the phase, we have constructed a polarizing interferometer that uses solid birefringent optical components (to obtain an appropriate mean optical delay offset ϕ_0) sandwiched between broadband (> 1 μm) wire grid, dielectric or crystal plate polarizers. The optical delay is given by $\tau = LB(\nu)/c$ where L is the thickness of the crystal in the direction of propagation and $B(\nu) = n_E(\nu) - n_O(\nu)$ is the crystal birefringence. If the crystals are also electro-optic, the birefringence, and hence the path length delay, can be modulated to generate a time varying signal at the detector. Alternatively, a separate electro-optic modulator can be used. An interference filter (or the natural passband of the optical components/detectors) is used to select the spectral region of interest. Light can be coupled to the instrument directly or using an optical fibre/collimating lens combination. A schematic of the electro-optic birefringent filter is given in Fig. 3

Both lithium niobate $LiNbO_3$ and lithium tantalate $LiTaO_3$ are potential modulator materials, being electro-optic and transparent from the visible through to 5 μm. Fig. 4 shows the infrared wavelength dependence of the absorption coefficients for both these materials. The crystals are also naturally birefringent (uniaxial) for light propagating along the crystal Y-axis (so called Y-cut). The birefrigence can be modified by applying an electric field in the Z-direction, parallel to the crystal fast axis, and transverse to the direction of propagation. For an applied electric field $E = V/d$, where V is the voltage across the crystal and d is the crystal aperture, the phase delay modulation for propagation along the crystal Y-axis is given by

$$\mu = \frac{\pi E L \nu}{c} \delta \tag{11}$$

where $\delta = (n_E^3 r_{33} - n_O^3 r_{13})$ and r_{33} and r_{13} are electro-optic tensor coefficients. The electro-optic modulation gives rise to a wavelength independent time delay $\tau = \mu/2\pi\nu = EL\delta/2c$.

Combining two such crystals with their fast axes mutually oriented at 90° but modulated with opposite polarity, will subtract their respective delays (to give a small nett delay ϕ_0) while adding the modulation component (to improve the modulation depth). The sinusoidal modulation drive voltage can be generated using a simple function generator, stereo audio amplifier and step-up transformer, with the modulation angular frequency Ω chosen to match the time resolution required by the application. The ac modulation can be superimposed on an

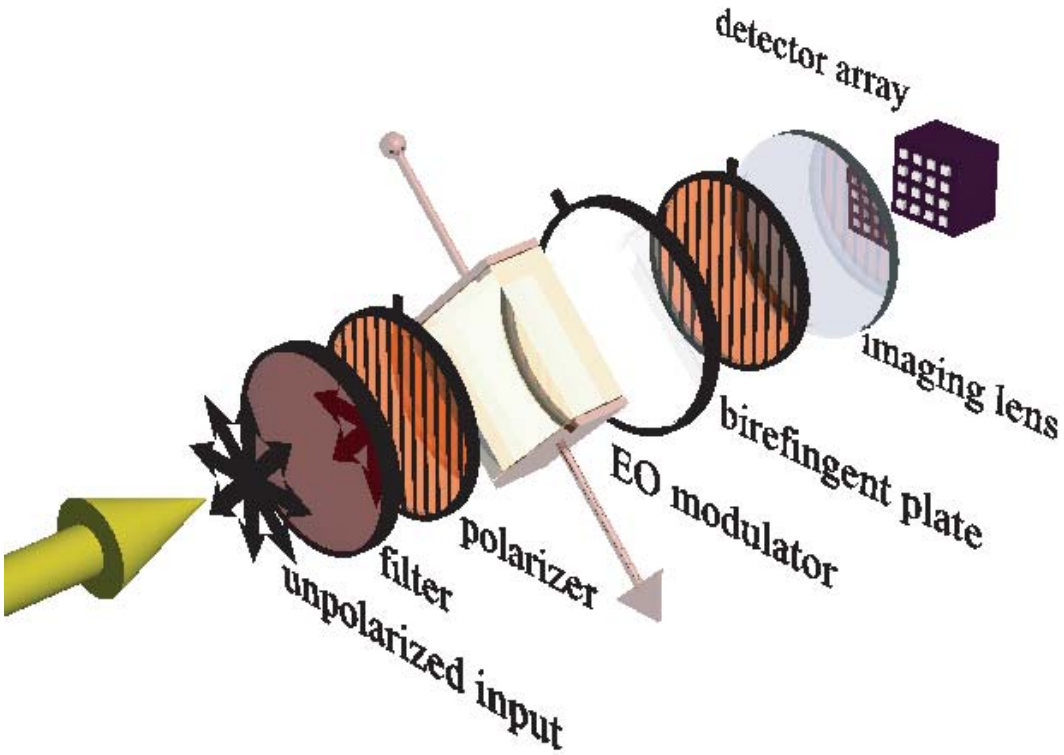

Figure 3: Optical layout for the Modulated Infrared Filter Spectrometer.

adjustable dc offset that allows some tuning of the waveplate delay offset, or "operating point". The EO tensor coefficients for both $LiNbO_3$ and $LiTaO_3$ are comparable, with $r_{33} \approx 30$ pm/V and $r_{13} \approx 8$ pm/V. For $d = 20$ mm aperture optics, an applied voltage of 4000V across a plate of thickness $L \approx 20$ mm will generate a phase modulation amplitude of 48° at 3 μm.

Because the required net optical path length delays may be only a few waves or so, $LiTaO_3$ which is weakly birefringent (B=.0045 at 3μm), would appear to be the more suitable candidate for infrared electro-optic applications. Tolerances on crystal thicknesses are modest and small crystal delays allow a wide field-of-view. However, the birefringence for $LiTaO_3$ is quite temperature sensitive, and the crystal would require to be temperature controlled for applications requiring long-term optical path length stability.

An alternative to crossed Y-cut birefringent plates is to propagate the light along the electro-optic plate Z-axis (Z-cut). In this case, there is no natural birefringence for on-axis rays, so that any required nett optical delay ϕ_0 must be introduced using additional fixed delay Y-cut birefringent plates (see Fig. 3). Nevertheless, an electric field applied along the Y-axis of the Z-cut crystal, will induce a birefringence that can be used to modulate the path length or tune the

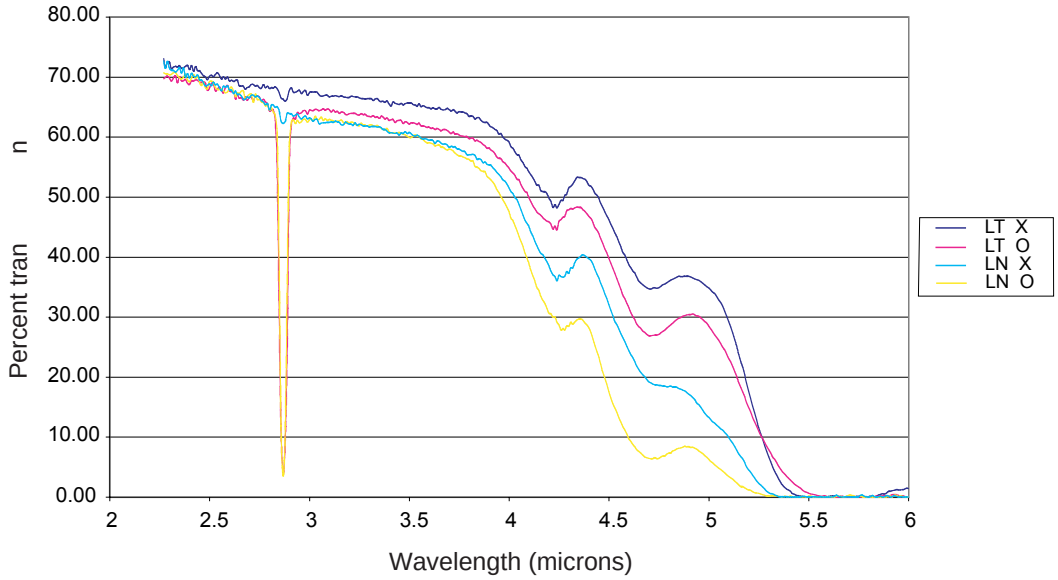

Figure 4: Wavelength dependence of lithium niobate and lithium tantalate transmission through 20mm thick Y-cut crystal plates for both ordinary and extraordinary waves (courtesy Defence Science and Technology Organisation, Salisbury, South Australia).

offset delay. The delay is given by [5].

$$\mu = \frac{\pi E L \nu}{c} 4 n_o^3 r_{22} \tag{12}$$

With $r_{22} \approx 3.4$ pm/V for $LiNbO_3$, the drive voltages need to be 30% higher than for crossed Y-cut crystals. The situation is much poorer for $LiTaO_3$ for which $r_{22} \approx -0.2$ pm/V so that this approach would necessitate the use of $LiNbO_3$ plates. Because of the higher natural birefringence for off-axis rays, the modulator would still require to be field-widened for imaging applications. However, the zero nett delay offset would be stable, allowing thermally compensated fixed wave plates to be used to obtain the required fixed optical delay.

Apart from $LiNbO_3$ and $LiTaO_3$, there are a number of other IR-transmissive birefringent materials suitable for the construction of fixed waveplates. Magnesium fluoride (high transmission from 100-8000 nm) is attractive because of its low refractive index (1.35) and small, reasonably achromatic birefringence ($B \approx 0.01$) and modest temperature coefficient $\mathrm{d}B/\mathrm{d}T = -0.6 \times 10^{-6}$/K (see Fig. 5). Combining waveplates having different material properties allows the construction of thermally stable compound plates as discussed in Sec. 6.3.

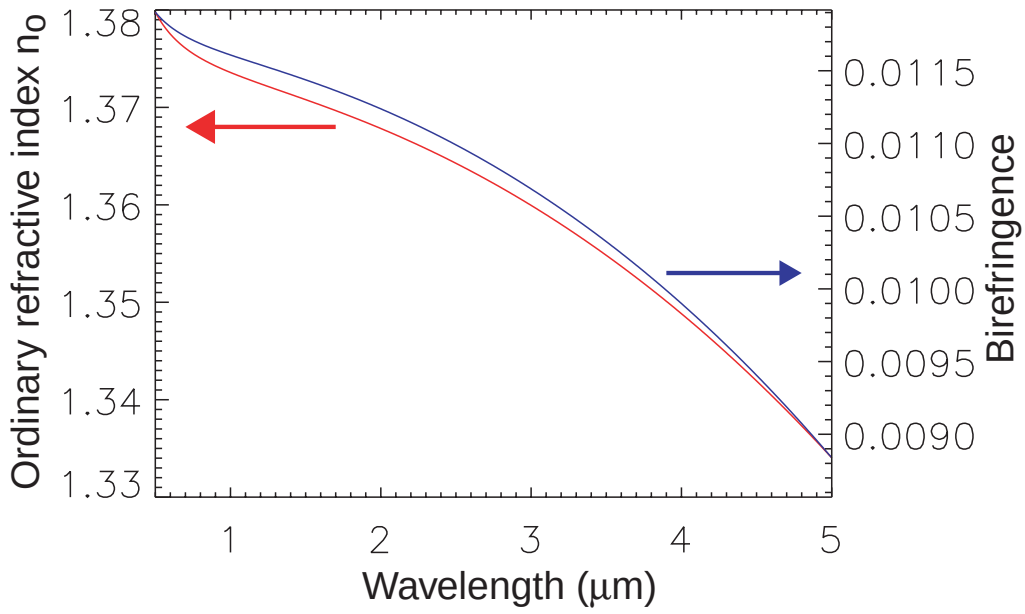

Figure 5: Wavelength dependence of ordinary refractive index and birefringence for magnesium fluoride.

5 Theoretical analysis

The change in the spectral centre-of-mass with temperature is manifest as a change in the interferogram carrier frequency. The variation gives rise to a temperature-dependent shift in the interferogram phase which increases with delay (see Fig. 1). The phase shift can be efficiently probed by electro-optically monitoring the position of a turning point or zero crossing that is offset some number of waves from zero delay. Changes in the interferogram phase are registered as a change in the frequency content of the modulation signal.

5.1 Linear approximation

When the emissivity varies strongly with wavelength, it may be desirable to limit the observed spectrum to a region which conforms to the blackbody law. For example, in the mid-IR, where atmospheric effects can be difficult to quantify, it may be advantageous to restrict observation to the wavelength range from 3-4 μm. Over a sufficiently narrow spectral region it is valid to linearly approximate

the blackbody spectral radiance at optical frequency $\nu = \nu_0 + \delta\nu$:

$$H_\nu(\nu) \approx H_0 \left[1 + \beta(x_0)\frac{\delta\nu}{\nu_0}\right] \tag{13}$$

where

$$\begin{aligned} \beta(x_0) &= \frac{x_0}{H_0}\frac{\partial H}{\partial x}\,|_{x_0} \\ &= 3 - \rho_0 \end{aligned} \tag{14}$$

with $x_0 = h\nu_0/kT$, $H_0 \equiv H_\nu(x_0)$ and $\rho_0 = \rho(x_0)$ given by Eq. (7) (see also Fig. 2). Substituting Eq. (13) into Eq. (10) and evaluating the integral gives the interferogram coherence

$$\gamma(\tau, \Delta\nu; T) = \zeta_T(\tau, \Delta\nu)\cos[\phi_0 + \phi_T(\tau, \Delta\nu)] \tag{15}$$

where τ is the interferometer time delay and the temperature-dependent interferogram phase shift is given approximately by

$$\tan\phi_T = (\rho_0 - 3)\frac{\phi_0}{3}(1 + \kappa_0)\left(\frac{\Delta\nu}{\nu_0}\right)^2 \equiv (\rho_0 - 3)\frac{\hat{\phi}_0}{3}\frac{\Delta\nu}{\nu_0} \tag{16}$$

where

$$\hat{\phi}_0 \equiv \phi_0(1 + \kappa_0)(\Delta\nu/\nu_0) \tag{17}$$

is a scaled phase shift coordinate proportional to the centre frequency phase delay $\phi_0 = 2\pi\nu_0\tau$. The factor

$$\kappa_0 = \frac{\nu_0}{B}\frac{\partial B}{\partial \nu}\,|_{\nu_0} \tag{18}$$

accounts for the wavelength dependence of the birefringence, while $\Delta\nu$ is half the optical bandwidth of the received radiation. Expression (16) is valid provided $\hat{\phi}_0^2/15 \ll 1$. To lowest order, the phase shift is zero when $\rho_0 = 3$ corresponding to the peak of the blackbody curve ($\rho_{\text{peak}} = 2.822$). For small ϕ_T, the total interferogram phase is given by $\phi_0 + \phi_T = 2\pi\nu_T\tau$ where the fringe frequency depends on the spectral centre of mass as determined by the source temperature.

While the fringe frequency changes with temperature, the fringe contrast envelope falls quadratically with delay

$$\zeta_T(\tau, \Delta\nu) = 1 - \frac{\hat{\phi}_0^2}{6} \tag{19}$$

and is insensitive to the temperature to lowest order in $\Delta\nu/\nu_0$. As expected, this result shows that the coherence length (the required delay for a significant reduction in fringe contrast) is inversely proportional to the width of the optical passband. The choice of delay offset (operating point) ϕ_0 is a balance between

the loss of fringe contrast attending large delay and the temperature-dependent phase shift ϕ_T which increases with $\hat{\phi}_0$.

When operating at infrared wavelengths, and for reasonable crystal dimensions and applied voltages, the phase modulation amplitude $\mu = \mu_0 + \mu_1 \sin \Omega t$ is generally small ($\lesssim 1$). Under these conditions, we combine Eqs. (15) and (9) for the interferometer signal and use the Bessel expansion to obtain

$$S = \frac{I_0}{2} \left[1 + J_0(\mu_1)\zeta_c - 2J_1(\mu_1)\zeta_s \sin \Omega t + 2J_2(\mu_1)\zeta_c \cos 2\Omega t\right] \tag{20}$$

where $I_0 = H_\nu(\nu_0)\Delta\nu$ is the spectrally integrated radiant power in the measurement passband, $(\zeta_c, \zeta_s) = \zeta_T[\cos(\phi_T + \phi_0), \sin(\phi_T + \phi_0)]$ and we have taken the applied dc phase bias $\mu_0 = 0$. The phase modulation amplitude μ_1 is given by Eq. (12) with frequency ν_0.

For modulation about a peak in the interferogram, the modulation signal predominantly occurs at twice the modulation rate (second harmonic). When the temperature changes, the peak (or trough) position also shifts. The generated signal registers this as a change in the ratio of fundamental and second harmonic amplitudes. The tangent of the appropriately weighted second and first harmonic amplitudes measures the phase in the modulation cycle at which the interferogram turning point (related to λ_M) is encountered. An important advantage of this measurement scheme is that the desired information is shifted onto carriers displaced from dc. As seen in Fig. 1, the position of the interferogram zero crossing also shifts with temperature. In this case, the information can be extracted from the ratio of the fundamental (modulation amplitude) and dc signal components. The relative sensitivity of the two alternatives is assessed below.

The analytic results obtained above have been tested numerically. For a given applied electric field, we calculate the frequency dependent phase delay Eq. (11) together with the appropriately filtered ideal blackbody spectral radiance H_ν and compute the resulting Fourier transform using Eq. (10). As an example we show normalized blackbody spectra for temperatures in the range 600K to 1000K [Fig. 6(a)] and their associated interferograms [Fig. 6(b)] after filtering by an ideal narrow bandpass filter transmitting between 3.25 and 3.75 μm ($\Delta\nu/\nu_0 = 1/14$). The interferogram is plotted as a function of the thickness of a magnesium fluoride waveplate ($\kappa_0 = 0.267$).

5.2 Measurement strategy

Using Eq. (20), the fundamental and second harmonic amplitudes are obtained as

$$S_1 = I_0\zeta_T(\tau)J_1(\mu_1)\sin\phi_T \tag{21}$$

$$S_2 = I_0\zeta_T(\tau)J_2(\mu_1)\cos\phi_T \tag{22}$$

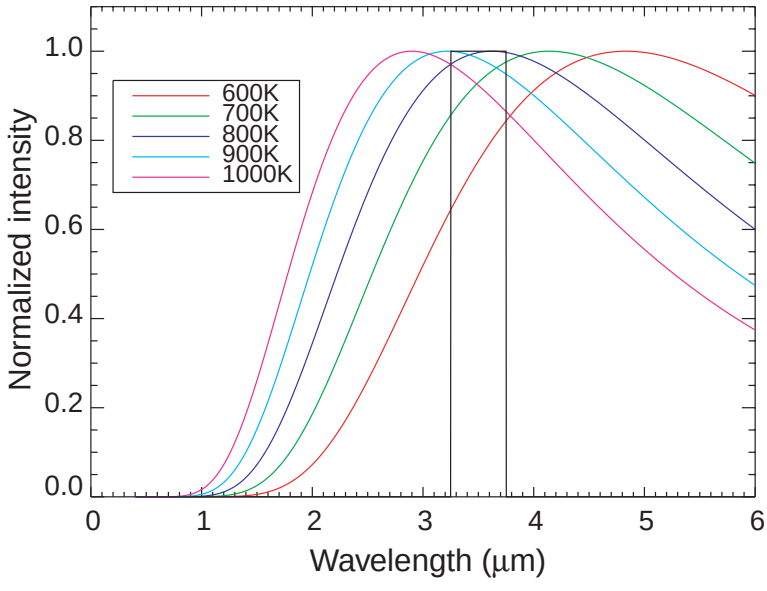

(a)

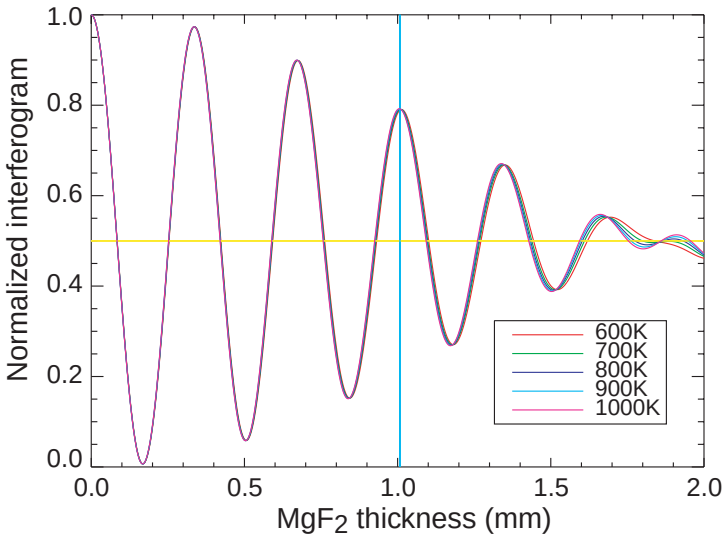

(b)

Figure 6: (a) Normalized blackbody spectra for temperatures in the range 600K to 1000K and superimposed ideal bandpass filter; (b) the corresponding interferograms for passband 3.25-3.75 μm

where we have taken $\phi_0 \equiv \phi_0^{(n)} = 2\pi\nu_0\tau_n$ where $\tau_n = n/\nu_0$ corresponding to modulation about the nth interferogram peak. The weighted ratio of the harmonic amplitudes is related to the source temperature through its dependence on the sensitivty factor ρ_0 (see Fig. 2(a)):

$$Q = \frac{J_2(\mu_1)S_1}{J_1(\mu_1)S_2} = \tan\phi_T \;=\; (\rho_0 - 3)\frac{\hat{\phi}_0}{3}\left(\frac{\Delta\nu}{\nu_0}\right). \tag{23}$$

It is very significant that in forming the harmonic ratio to obtain ϕ_T we remove any dependence on the the emission intensity or the fringe contrast (including instrumental components). For the conditions of Fig. 6 we have computed the time domain signal S for delay offset $\phi_0^{(3)}$ and extracted the harmonic components S_1 and S_2. The vertical line in Fig. 6(b) coincides with the $n = 3$ peak. In this case the temperature variation of the numerically and analytically calculated weighted ratios of the second harmonic and fundamental amplitudes are compared in Fig. 7. The discrepancy is due to breakdown of the low order approximations involved in obtaining the analytic expression. For modulation about the first peak (where $\hat{\phi}_0$ is small) the correspondence is very close.

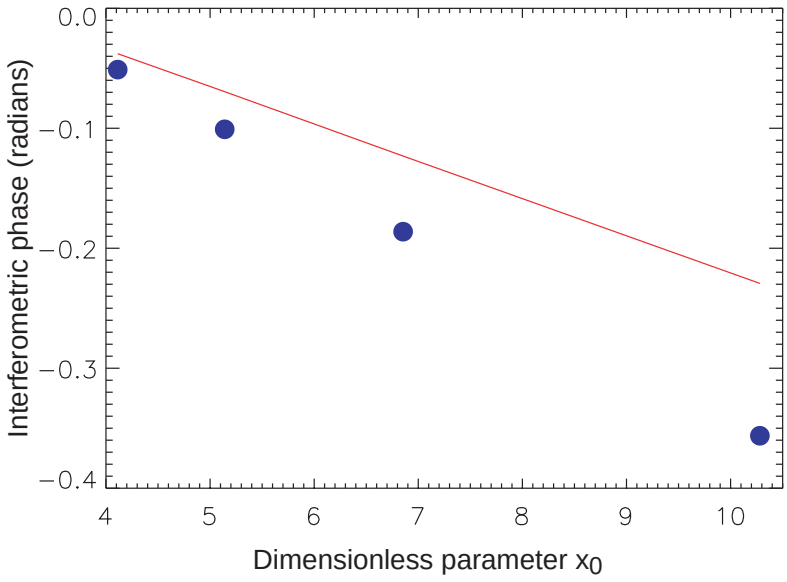

Figure 7: The calculated (squares) and analytically approximated temperature dependent phase shift for measurements centred on the third interferogram peak shown in Fig. 6(b). See text for discussion.

Noise sensitivity

For a given temperature range, it is important to determine the parameters ν_0, $\Delta\nu$, μ_1 and $\phi^{(n)}$ which optimize the signal-to-noise ratio. For IR measurements, we assume that the SNR is dominated by detector noise of rms amplitude ε in a given detection bandwidth Δf about each of the harmonic carriers. With the random noise component included in Eqs. (21) and (22), the associated rms noise on Q is given by

$$\varepsilon_Q = \frac{\varepsilon}{I_0\,\zeta_T\,\chi} \tag{24}$$

where the factor χ depends on the temperature-dependent phase shift ϕ_T and the modulation index μ_1

$$\chi = \frac{J_1(\mu_1)J_2(\mu_1)\cos^2\phi_T}{[J_2^2(\mu_1)\cos^2\phi_T + J_1^2(\mu_1)\sin^2\phi_T]^{1/2}}. \tag{25}$$

For uncertainty ΔQ in the ratio estimate Q (due for example to detector noise ε), we can use Eq. (23) to obtain an estimate for the corresponding uncertainty ΔT_Q in the inferred temperature:

$$\Delta Q = \rho_0 \frac{\hat{\phi}_0}{3}\frac{\Delta\nu}{\nu_0}\left(\frac{T}{\rho_0}\frac{\partial\rho}{\partial T}\mid_{x_0}\right)\frac{\Delta T_Q}{T}. \tag{26}$$

It is straightforward to show that

$$\frac{T}{\rho_0}\frac{\partial\rho}{\partial T}\mid_{x_0} = x_0 - \rho_0 + 1 \approx 1 \tag{27}$$

across most of the blackbody spectrum (see Fig. 2). Equating the uncertainty ΔQ with the measurement error ε_Q given by Eq. (24) and using Eq. (6) to link the signal to noise ratio I_0/ε and the radiometric temperature uncertainty ΔT_R finally gives

$$\eta_Q \equiv \frac{\Delta T_R}{\Delta T_Q} \;=\; \zeta_T\,\chi\,\frac{\hat{\phi}_0}{3}\left(\frac{\Delta\nu}{\nu_0}\right) \tag{28}$$

The apparently linear dependence of sensitivity η_Q on phase delay ϕ_0, is offset by the decrease in fringe contrast ζ_T given by Eq. (19). On differentiation, the optimum operating point occurs at $\hat{\phi}_0 = \phi_0(1+\kappa)(\Delta\nu/\nu_0) = \sqrt{2}$, just within the range of validity of the approximations leading to expressions (16) and (19) for ϕ_T and ζ_T. We choose the nearest peak to this optimum operating point and substitute into Eq. (28) to obtain

$$\eta_Q = \frac{2\sqrt{2}}{9}\chi\left(\frac{\Delta\nu}{\nu_0}\right) \tag{29}$$

Finally, the extent to which the harmonic components are efficiently generated depends on the modulation index μ_1 through the factor χ. This factor is maximized by modulating about a peak obtained by adjusting the applied dc offset μ_0 such that $\phi_T = 0$. (One might also envision a system in which the dc bias is automatically adjusted to minimize the fundamental signal component, thereby directly reading out the temperature.) With this condition, and using the small angle expansion for $J_1(\mu_1)$, we finally obtain the relative temperature sensitivity

$$\eta_Q \approx 0.16\mu_1\left(\frac{\Delta\nu}{\nu_0}\right) \tag{30}$$

It is reasonable to expect that methods based on simple spectral estimates are less sensitive at least by the fractional bandwidth $\Delta\nu/\nu_0$. Note that the relative sensitivity is independent of the normalized optical frequency x. As for radiometric sensing, this implies that the optimum operating frequency band should be located near $x = 4$.

Probing zero crossings

We compare the filter performance in the case of modulation about interferogram zero crossings with the the peak probing strategy. For the nth interferogram zero crossing $\phi_0^{(n)} = 2\pi\nu_0\tau_n$ with $\tau_n = (2n+1)/4\nu_0$, the dc and fundamental signal amplitudes are given by Eq. (20)

$$\begin{aligned} S_0 &= I_0/2\,[1 + \zeta_T J_0(\mu_1)\sin\phi_T] \\ S_1 &= -I_0\zeta_T J_1(\mu_1)\cos\phi_T. \end{aligned}$$

Assuming the phase shift ϕ_T is small, it is possible to express the temperature dependent phase shift ϕ_T in terms of the contrast ζ_T and the ratio of the harmonic amplitudes $R_{10} = S_1/S_0$ as

$$Q = \frac{R_{10} - 2\zeta_T J_1(\mu_1)}{2\zeta_T^2 J_1(\mu_1) J_0(\mu_1)} \;\approx\; \phi_T \tag{31}$$

In this case, the calculation requires knowledge of the fringe contrast ζ_T, which in practice, would also include an instrumental component. This is not the case for peak probing, where the the instrument component is eliminated on taking the harmonic ratio. The attendant noise is calculated as

$$\varepsilon_Q = \frac{\varepsilon}{I_0\zeta_T^2 J_1(\mu_1)} \tag{32}$$

valid to lowest order in the small quantites μ_1 and ϕ_T. As for the peak modulation case, we calculate the sensitivity relative to direct radiometric detection:

$$\eta_Q \equiv \frac{\Delta T_R}{\Delta T_Q} \;=\; \zeta_T^2\, J_1(\mu_1)\, \frac{\hat{\phi}_0}{3} \left(\frac{\Delta\nu}{\nu_0}\right) \tag{33}$$

As the contrast decreases with delay ϕ_0, so also does the available modulation depth. This gives rise to a squared dependence of the relative sensitivity on the contrast $\zeta_T < 1$. The optimum operating point is now given by $\hat{\phi}_0 = 1$ and the relative sensitivity is slightly poorer than for the peak modulation case:

$$\eta_Q = 0.11\mu_1 \left(\frac{\Delta\nu}{\nu_0}\right) \tag{34}$$

5.3 Interferometric ratio methods

To be addressed.

6 Calibration and non-ideal effects

The sensitivity of MIRF to temperature changes arises because the two lowest order moments of the spectrum dominate the interferogram at small delay. If these two spectral averages are not strongly distorted, the temperature sensitivity of the system is robust and can be quantified through calibration against a known greybody having its temperature independently determined using contact sensors.

A number of effects can distort the temperature dependent phase shift or complicate interpretation.

(a) The emissivity may vary with wavelength in the observation passband (non-greybody). Assuming the variation is known, it can be compensated by applying a "slope" factor that will correct the slope of the linear relationship between ϕ_T and x.

(b) For moderate path lengths, atmospheric absorption effects can modify the blackbody spectrum. The effect can generally be avoided with appropriate choice of infrared or visible passband.

(c) Optical components can display a spectrally varying attenuation and birefringence, while detector response can also vary sharply across the passband. These effects can be accommodated through careful instrument calibration.

(d) Reflections form a higher temperature background can be problematic. Measurements made simulatneously at multiple optical delays may allow these effects to be compensated.

(e) Environmental degradation of instrument performance. This can include contamination of optical surfaces and thermal variation of optical component refractivity.

6.1 Spectral distortion

To illustrate the robustness of the phase shift measure of temperature variation, we allow for the spectral distortion resulting from attenuation through a 20mm $LiNbO_3$ plate and include the wavelength dependence of a Peltier cooled PbSe detector. The radiation bandwidth is assumed to be limited by a bandpass filter centred at 4.25 μm with full width half maximum (FWHM) 0.5 μm and Lorentzian lineshape. The resulting calculated non-ideal spectral filter transmission is shown in Fig. 8 (a). For comparison is shown an ideal top-hat filter with centre at 4 μm and FWHM 0.7 μm. The associated interferograms for blackbody radiation at 700 K are shown in Fig. 8 (b). The contrast is poorer for the broader band non-ideal filter, while the interferogram period is smaller, consistent with the greater weighting of shorter wavelength radiation. The vertical line coincides

with the operating point which is taken to coincide with the $n = 3$ peak of the "ideal" interferogram.

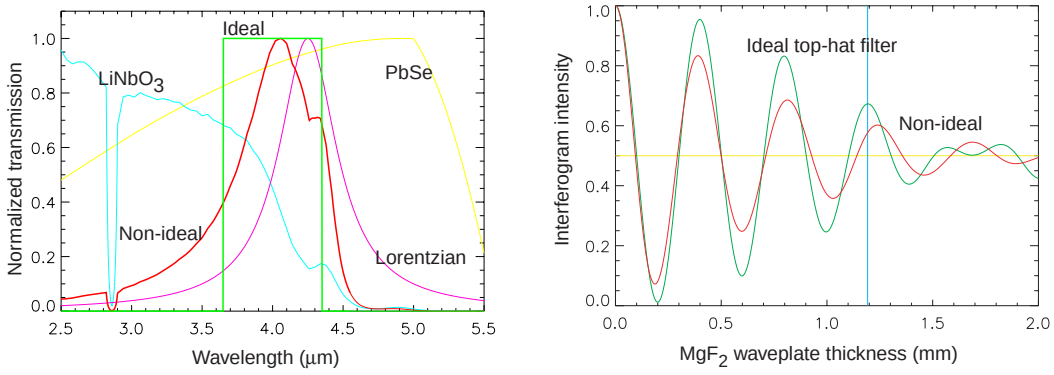

(a) (b)

Figure 8: (a) Ideal (top-hat) and non-ideal filter functions used to model MIRF response. The non-ideal curve is the product of the detector response (PbSe), the crystal transmission function ($LiNbO_3$) and a Lorentzian bandpass filter centred on 4.25 μm. (b) The computed interferograms in each case for a blackbody source at 700 K. The vertical line is the selected operating point (waveplate delay) about which the optical path length is modulated. See text for discussion.

The contraction of the interferogram for the non-ideal filter results in an offset in the inferred phase ϕ_T from that obtained in the ideal case. This is shown in Fig. 9 where the phase shift ϕ_T inferred from the weighted fundamental to second harmonic ratio is plotted against normalized coordinate x_0 for the temperature range 400, (100), 1000 K with $\lambda_0 = 4\,\mu$m. Despite the significant phase shift and the change in slope (due to the different passband widths) there remains an approximately linear relationship between the interferogram phase delay and the dimensionless wavenumber x_0. The departures from the idealised case can be determined through a one-off system calibration against a greybody of known temperature.

6.2 Unfolding background effects

The object of interest can also reflect radiation within its environment giving rise to a total radiance

$$H(\nu) = \epsilon H_\nu(\nu; T_{\text{obj}}) + (1 - \epsilon) H_\nu(\nu; T_{\text{amb}}) \tag{35}$$

More to come ...

6.3 Environmental effects

Radiometric thermometers are often required to operate in close proximity to harsh environments such as furnaces. It is therefore important to consider the

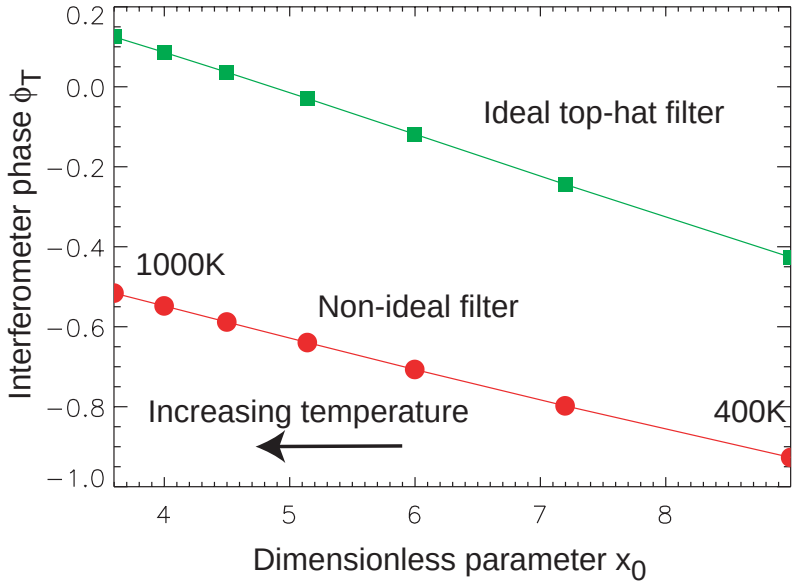

Figure 9: The dependence of the inferred interferometric phase on source temperature (normalized coordinate x_0) for the ideal and non-ideal filter cases. See text for discussion.

temperature stability of the optical delay set by the waveplate. Magnesium fluoride crystals exhibit a modest temperature coefficient $\mathrm{d}B/\mathrm{d}T = -0.6 \times 10^{-6}/\mathrm{K}$. Nevertheless, this corresponds to a fractional change in waveplate delay of 0.6% for a temperature change of 100K, resulting in a not insignificant phase drift of 0.1 radians when monitoring the $n = 3$ peak.

A simple approach is to compensate the drift using a crystal having different properties. Cadmium sulphide is suitable for this purpose, being transmissive from 0.6-14 microns, having modest birefringence $\sim .015$ and temperature coefficient $\mathrm{d}B/\mathrm{d}T = 3.1 \times 10^{-6}/\mathrm{K}$ (`www.clevelandcrystals.com`). For a prescribed delay offset ϕ_0 the crystal thicknesses are determined by solving the trivial simultaneous equations

$$\begin{aligned} \phi_{01} + \phi_{02} &= \phi_0 \\ c_1\phi_{01} + c_2\phi_{02} &= 0 \end{aligned}$$

where the birefringent phase delay introduced by the ith plate is given by $\phi_{0i} = 2\pi L_i B_i/\lambda_0$ and the temperature coefficients are given by $c_i = (\partial B_i/\partial T)/B_i$. Negative crystal lengths imply simply that the crystal Z axes should be orthogonal.

Should drifts remain problematic, the operating point can be routinely monitored using a fixed temperature greybody source. The reference radiation can be injected via the first polarizing splitter reject port and gated using a shutter.

6.4 Dynamic range

When using the blue side of the Planck blackbody curve, it is clear that the power captured within a given passband will increase rapidly with temperature. This is both beacuse the radiant intensity is proportional to T^4 and because the spectrum peak shifts further into the measurement passband. As noted above, montioring systems which exhibit significant temperature variation, requires special measures to handle the wide intensity dynamic range.

An alternative strategy is to monitor the red wing of the spectrum. In this case, though the radiant intensity still increases dramatically with temperature, the spectral peak moves out of the passband. The received blackbody radiant power in the bands $2-5\,\mu$m and $0.6-1.2\,\mu$m as a function of temperature is shown in Fig. 10. The reduction in required intensity dynamic range is clearly evident. The effect is even more pronounced when the red-weighted sensitivity of the semiconductor detectors is included. Red wing measurements, while technically more demanding and expensive, offer some advantage for measurements requiring high dynamic range. However, sensitivity to temperature changes is poorer because the relatively slow spectral roll-off makes spectral discriminiation more difficult.

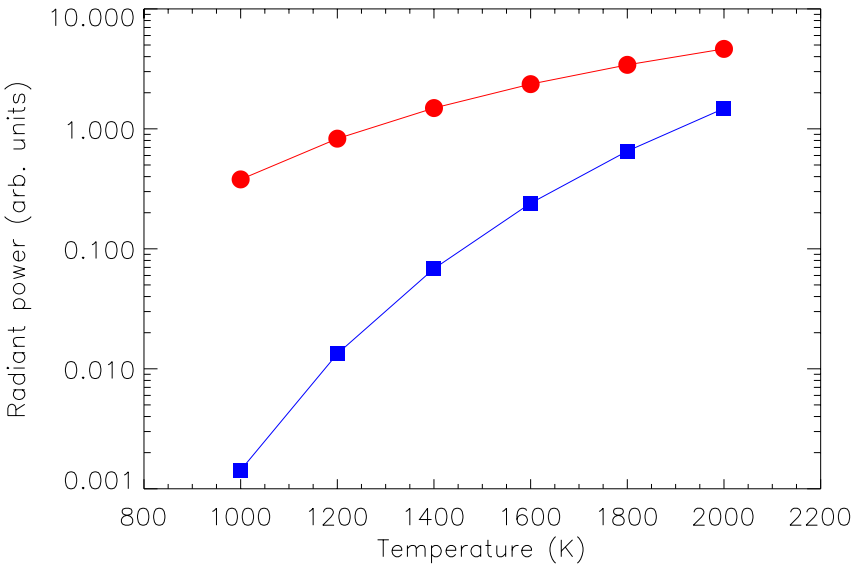

Figure 10: The variation of received power with temperature for red passband $2-5\,\mu$m (circles) and blue $0.6-1.2\,\mu$m (squares). There is a significant dynamic range advantage for red wing measurements.

7 Experimental verification

We have set up an experiment using a 12V filament lamp source and MIRF spectrometer based on Y and Z-cut $LiNbO_3$ crystals of length 50mm and aperture 25mm interposed between two broadband red-optimized (620-1000nm) polarizing beamsplitter cubes. A Hamamatsu red-sensitive GaAs photomultipler tube (R943-02, 200-900nm) was used as detector. A PC-based DAQ card operating under "PCMOSS"software control was used in conjunction with a high voltage amplifier to generate the modulating voltage (200Hz) applied to the crystals. The signals were synchronously acquired using the same PC-based DAQ system.

Figure 11(a) shows a portion of the interferogram measured by applying a linear ramp of peak amplitude 4000V across two 50mm Y-cut $LiNbO_3$ crystals. Apertures of $\sim 3-5$ mm diameter were used to limit the light flux and to improve instrument fringe contrast. The latter is an issue only for these preliminary experiments where compensating birefringent plates were unavailable (see Sec. 8.1). A bias offset of -2000V was required to compensate for a small mismatch in the crossed crystal lengths giving rise to incomplete dc cancellation of the optical path length. The bias allows a portion of the interferogram on both sides of the "white light" position (corresponding to zero net delay) to be measured. The interferograms have been arbitrarily normalized according to their minimum and maximum peak values. For comparison, Fig 11(b) shows calculated interferograms for a range of blackbody temperatures, assuming that only radiation in the band 600-900nm contributes to the interference signal. There is close similarity between measured and computed interferograms, including reasonable agreement about the electro-optic drive voltages required to probe the interferogram. The discrepancy may be due to the choice of effective optical bandwidth which has been used for the calculations.

The interferogram can be locally probed for sensitivity to temperature variations. For this purpose, we use a Z-cut modulator and fixed wave plate to sample about the first interferogram trough. The path length probing is achieved using a 200Hz sinusoidal modulation of amplitude 2000V (approximately quarter wave at 750 nm) and offset 2000V. The current through the lamp and its voltage are monitored, together with the synchronously sampled modulated light signal. Using the PCMOSS system, we have slowly ($\sim$ 10s) swept the filament voltage while recording the interferogram. Fig. 12(a) shows the variation of filament resistance with applied voltage. There is a clear hysteresis associated with the heating and cooling cycle. Fig. 12(b) shows the emitted light intensity (a function of temperature) versus filament resistance (also a function of temperature). As expected the hysteresis effects have almost vanished. The filament temperature can be inferred from the resistance using the relation [6]:

$$T_R/T_{\rm RT} = (R/R_{\rm RT})^{0.8298} \tag{36}$$

where $R_{\rm RT}$ is the filament resistance at room temperature $T_{\rm RT}$.

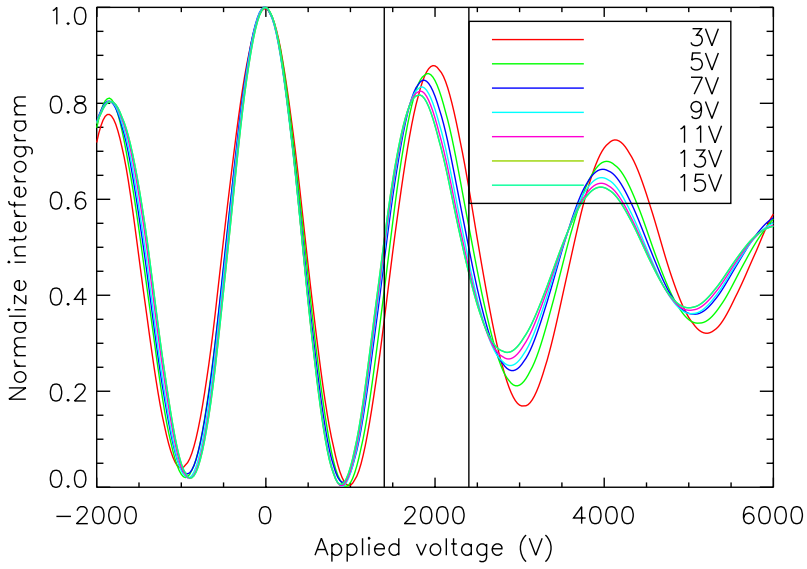

(a)

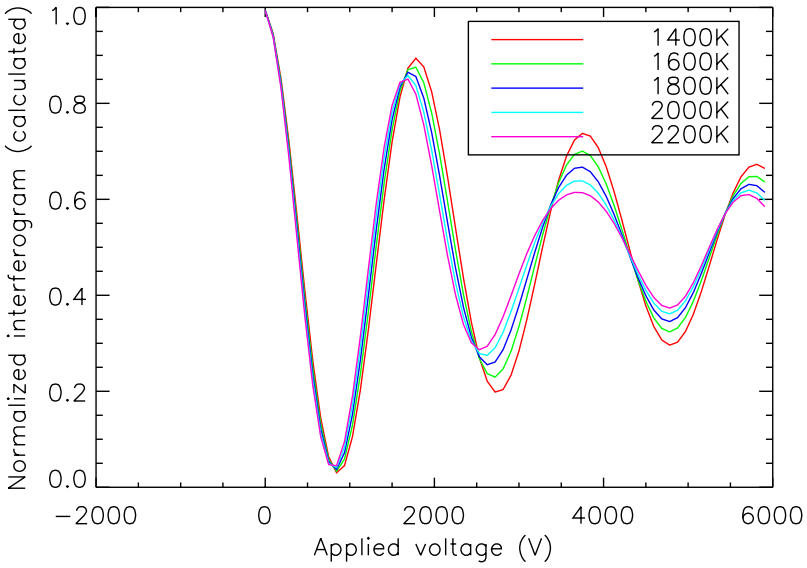

(b)

Figure 11: (a) Measured interferogram as a function of filament voltage and (b) computed interferograms for temperatures in the range 1400K to 2200K. See text for discussion.

The temeprature dependent phase ϕ_T calculated from the weighted ratio of fundamental and second harmonic amplitudes is plotted as a function of T_R in Fig. 13. The origin of the residual hysteresis is unknown at this time and may be a numerical artifact. This non-optimized system can resolve temperature changes of a few degrees Kelvin with excellent temporal resolution.

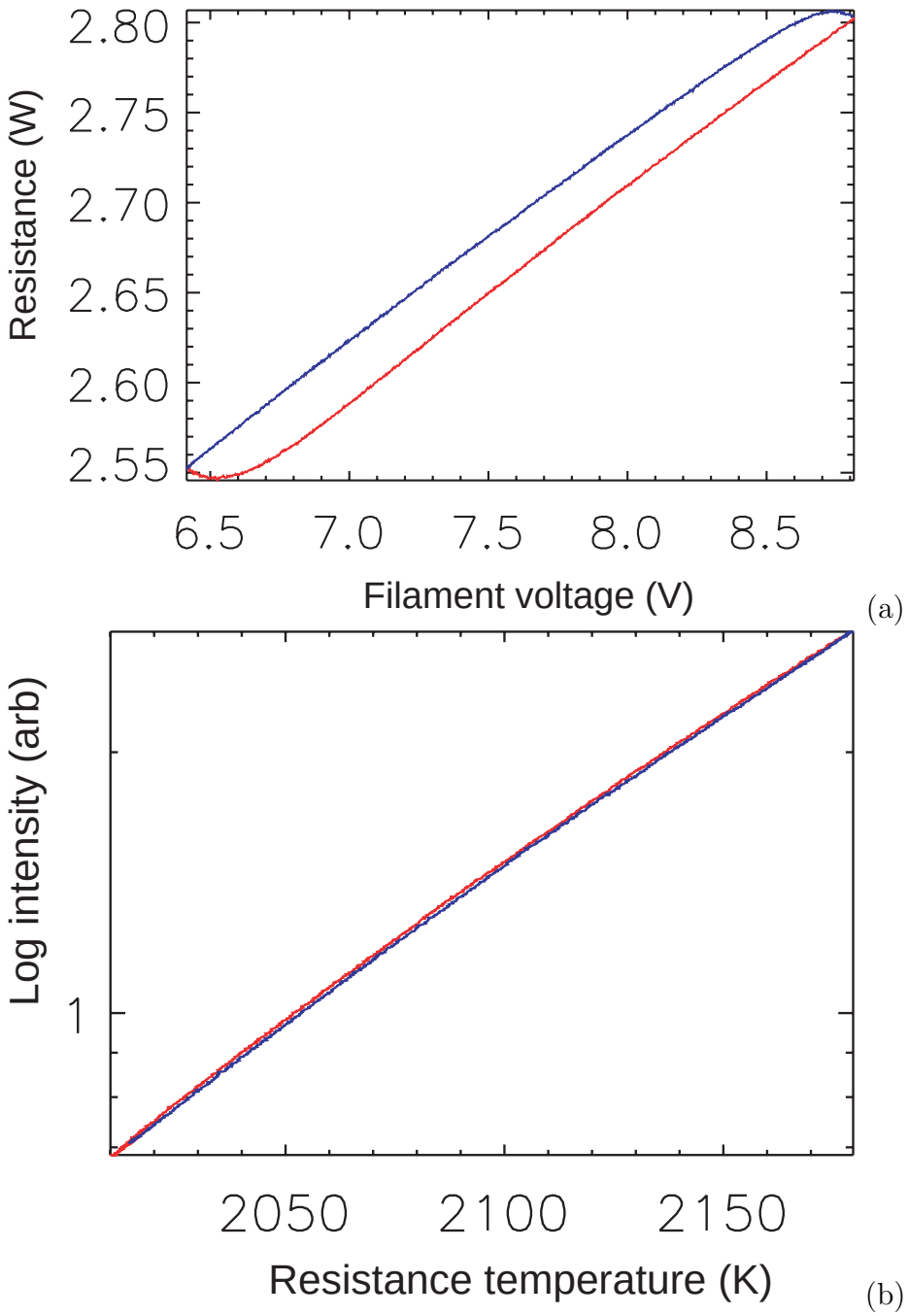

Figure 12: (a) Dependence of filament resistance on voltage during applied triangle voltage ramp of period 10 seconds. Observe the strongly hysteretic behaviour. (b) The light intensity (log scale) versus filament resistance indicates that the resistance is an approximately single valued measure of the instantaneous filament temperature.

8 MIRF infrared imaging thermography

Being a simple transmissive eo-modulated device, MIRF can be mounted as a prefilter to a standard mid-infrared imaging camera. Because the temperature

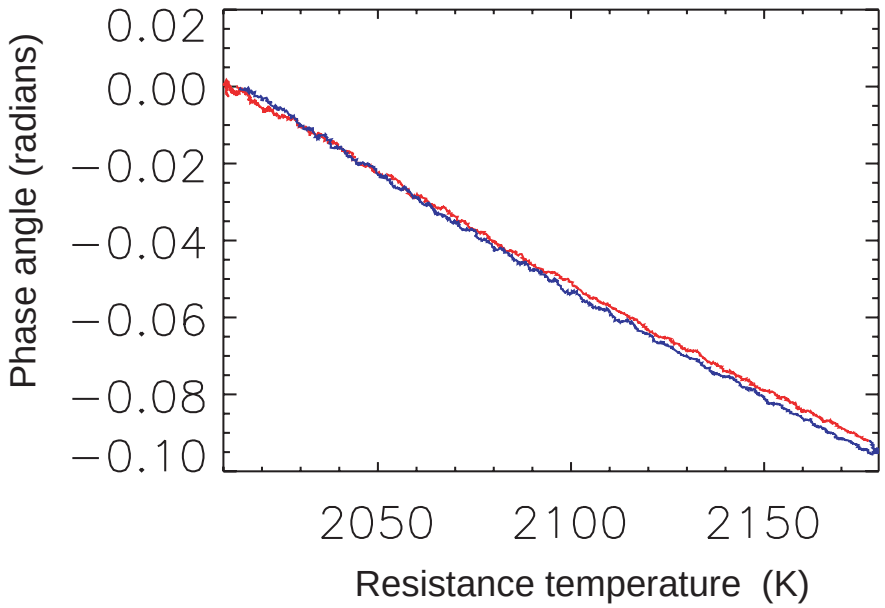

Figure 13: (a) The temperature-sensitive phase shift ϕ_T versus filament temperature inferred from measured filament voltage and current. See text..

can be extracted from the phase shift information, when combined with absolute intensity information that is also available, it may be possible to also determine the emissivity of objects in the field-of-view. This could be useful in various process monitoring applications.

A simple strategy for processing the modulated signals is to lock the modulation frequency to an integer submultiple of the camera frame rate. For example, to measure the harmonic ratios, it would be necessary to sample the interferometric image at four points in the modulation cycle. Algebraic manipulation of these frames using DSP hardware would yield the harmonic ratio image and hence the temperature distribution. In this case, the effective time resolution would be a quarter of the maximum CCD frame rate. The electronic hardware for processing and comparing sequential frames can stand independently of the camera, provided the camera makes the image digitally available.

8.1 Field-of-view

The average over the range of angles subtended by the source gives rise to an instrument contrast degradation that reduces the fringe visibility. This in turn results in decreased sensitivity for measurement of phase changes and an instrumental variation of dc phase offset ϕ_0.

For a free-space Michelson interferometer, the range of collected ray angles gives rise to a pattern of concentric rings in the interferometer image plane. Uniaxial Y-cut birefringent plates (such as MgF_2 or $LiNbO_3$) give rise to saddle-

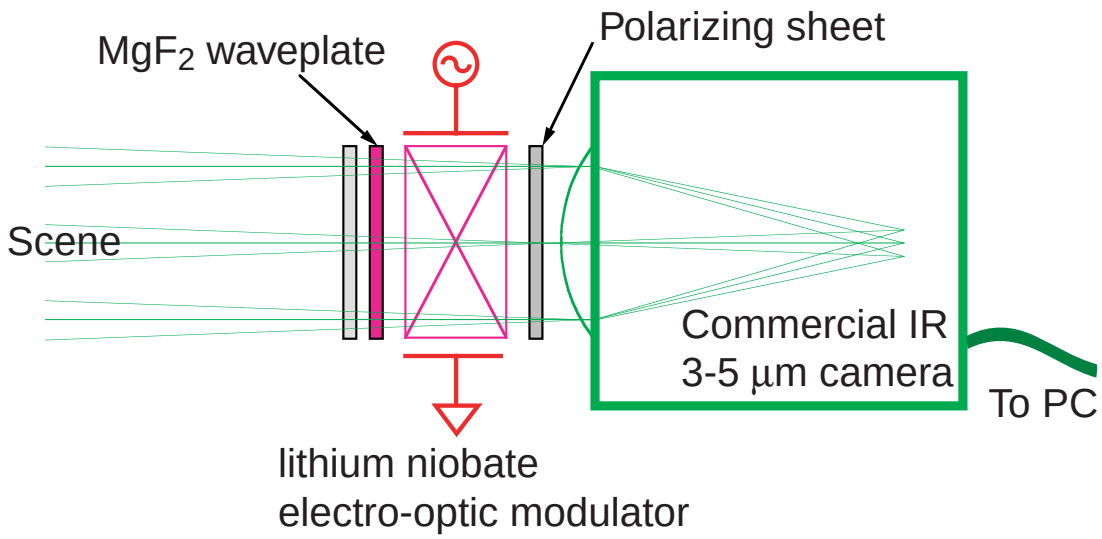

Figure 14: Scematic of optical layout for the imaging MIRF combined with commercial mid-IR digital camera.

like hyperbolic fringe patterns which are wavelength dependent. For small crystal delays, however, the field-of-view can exceed 30° without significant contrast degradation, while chromatic effects can be neglected. In any event, the field-of-view can be widened by using crossed birefringent crystals with an intervening half wave plate at an azimuth of 45° [7, 8].

To obtain the path length modulation requires the use of Z-cut electrooptic plates. For rays parallel to the Z-axis, there is no nett birefringence apart from that induced electrically. However, for off-axis rays, the crystal presents a residual birefringence with associated phase delay given approximately by [9]

$$\tilde{\phi} = \frac{2\pi\rho B\nu}{cn^2}\sin^2\vartheta \tag{37}$$

where ϑ is the ray angle of incidence and n is the mean refractive index. In general, the intensity transmitted by a birefringent filter having parallel polarizer and analyzer axes is given by

$$I = \frac{I_0}{2}[1 - \sin^2 2\psi \sin^2(\delta/2)] \tag{38}$$

where ψ is the angle between the first polarizer and the direction of vibration of the electric field in the

More discussion to follow regarding compensation of Z-cut modulator plates...

References

[1] P. C. Dufour, N. L. Rowell, and A. G. Steele, Appl. Opt. **37**, 5923 (1998).

[2] J. Howard, Appl. Opt. **41**, 197 (2002).

[3] J. Howard, C. Michael, F. Glass, and A. Cheetham, Rev. Sci. Instrum. **72**, 888 (2001).

[4] R. J. BELL, *Introductory Fourier Transform Spectroscopy* (Academic, New York, 1972).

[5] C. C. DAVIS, *Lasers and Electro-Optics* (Cambridge University Press, Cambridge, 1996).

[6] C.R.C. Handbook of Physics and Chemistry. Also see web site `http://faculty.millikin.edu/ jaskill.nsm.faculty.mu/exp42.html`.

[7] W. Steel, *Interferometry* (Cambridge University Press, Cambridge, 1967).

[8] C. Michael, J. Howard, and B. D. Blackwell, Rev. Sci. Instrum. **72**, 1034 (2001).

[9] M. BORN and E. WOLF, *Principles of Optics* (Pergamon Press, Oxford, 1980).